

Ultrathin Graphite Foam: A Three-Dimensional Conductive Network for Battery Electrodes

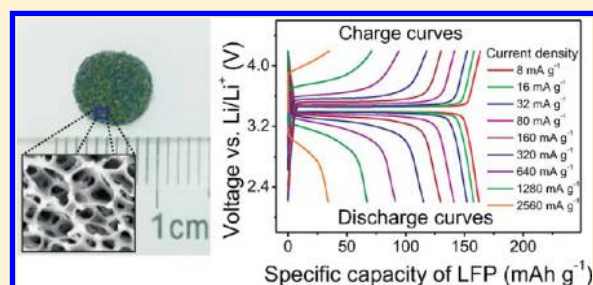
Hengxing Ji, Lili Zhang, Michael T. Pettes, Huifeng Li, Shanshan Chen, Li Shi, Richard Piner, and Rodney S. Ruoff*

Department of Mechanical Engineering and the Materials Science and Engineering Program, The University of Texas at Austin, 1 University Station C2200, Austin, Texas 78712, United States

Supporting Information

ABSTRACT: We report the use of free-standing, lightweight, and highly conductive ultrathin graphite foam (UGF), loaded with lithium iron phosphate (LFP), as a cathode in a lithium ion battery. At a high charge/discharge current density of 1280 mA g^{-1} , the specific capacity of the LFP loaded on UGF was 70 mAh g^{-1} , while LFP loaded on Al foil failed. Accounting for the total mass of the electrode, the maximum specific capacity of the UGF/LFP cathode was 23% higher than that of the Al/LFP cathode and 170% higher than that of the Ni-foam/LFP cathode. Using UGF, both a higher rate capability and specific capacity can be achieved simultaneously, owing to its conductive ($\sim 1.3 \times 10^5 \text{ S m}^{-1}$ at room temperature) and three-dimensional lightweight ($\sim 9.5 \text{ mg cm}^{-3}$) graphitic structure. Meanwhile, UGF presents excellent electrochemical stability comparing to that of Al and Ni foils, which are generally used as conductive substrates in lithium ion batteries. Moreover, preparation of the UGF electrode was facile, cost-effective, and compatible with various electrochemically active materials.

KEYWORDS: Graphite foam, three-dimensional electrode, conductive network, lithium ion battery



Advanced battery technologies are known to suffer from kinetic problems due to the low ion/electron conductivity of the electrode, especially for lithium (Li) ion technology.^{1–3} Approaches for enhancing the rate capability of batteries include developing new electrochemically active materials with high ion and electron conductivity,^{4,5} coating electrodes with a conductive layer,^{6–8} reducing the characteristic dimension of electrochemically active materials thereby reducing the ion diffusion time constant,^{9–12} and building up three-dimensional (3D) architected electrodes.^{13,14} Coating electrodes with a conductive layer, however, usually require somewhat complex chemical processes that are highly specific to the electrochemically active material.⁷ Nanoscale electrochemically active materials significantly improve the rate of lithium ion insertion/extraction, however, they yield low volumetric energy density due to their low tap density.⁹ In addition, the large electrode/electrolyte interface may lead to side reactions and serious safety issues.^{9,10}

An ideal electrode architecture consists of a 3D interconnected network of both electron and ion pathways to allow for efficient charge and mass exchange that occur when charging/discharging the battery.^{13,14} Inverse opal structures,^{15,16} coaxial nanostructures,^{17,18} mesoporous materials,^{19,20} and metal foam^{21,22} have been applied for this purpose. However, the electrochemically inactive material required for structural support significantly increases the mass and reduces the specific capacity of the electrode.^{13,14} Carbon materials, for example, carbon monolith,^{23,24} graphene,^{25,26} and carbon

nanotube,^{27–29} are popular conductive fillers for the electrode of a battery due to their low density and relatively good electrical conductivity. However, the rate capability usually depends on the distribution of these carbon fillers in the electrode, and the contact resistance between the fillers considerably limits the conductivity of the network. The fabrication of these electrode structures usually requires complex procedures depending on the specific electrochemically active material that is used. Moreover, the need of a metal current collector increases the total mass of the electrode. A simple electrode fabrication process with minimum (or little) increase of electrochemically inactive material that is compatible with the commercially available high-performance electrochemically active materials is thus highly desirable.

Here, we report fabrication of free-standing, lightweight, and highly conductive ultrathin graphite foams (UGFs) having a 3D interconnected structure. The UGF electrode can be combined with electrochemically active material by techniques commonly used in the battery industry and is applicable to various electrochemically active materials that are commercially available. We observe an enhanced specific capacity and rate capability simultaneously of the lithium iron phosphate (LFP) loaded on UGF owing to its lightweight, 3D conductive interconnected network, where the density of UGF is $\sim 9.5 \text{ mg cm}^{-3}$

Received: February 8, 2012

Revised: April 21, 2012

Published: April 23, 2012

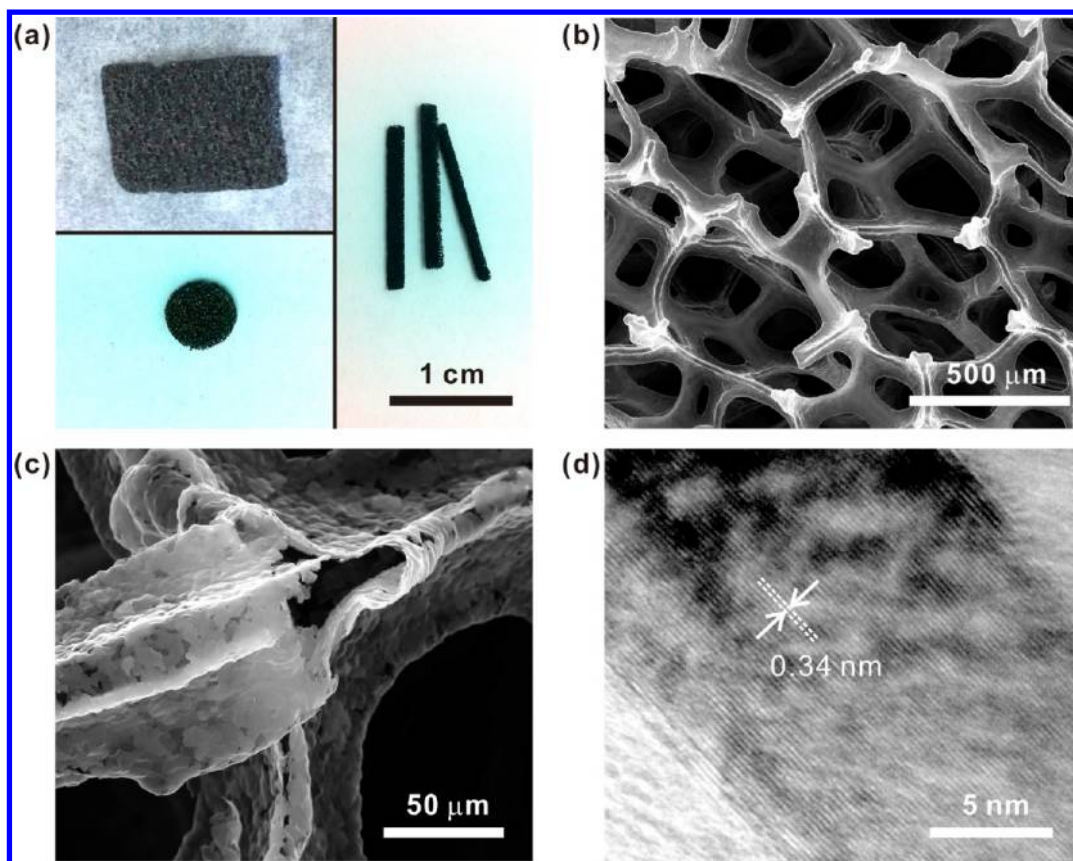


Figure 1. (a) Photograph of UGFs in different geometries. (b) SEM image of the UGF showing the microstructure of the UGF. (c) SEM image of a broken strut within the UGF; note the hollow, triangular structure. (d) TEM image of the UGF.

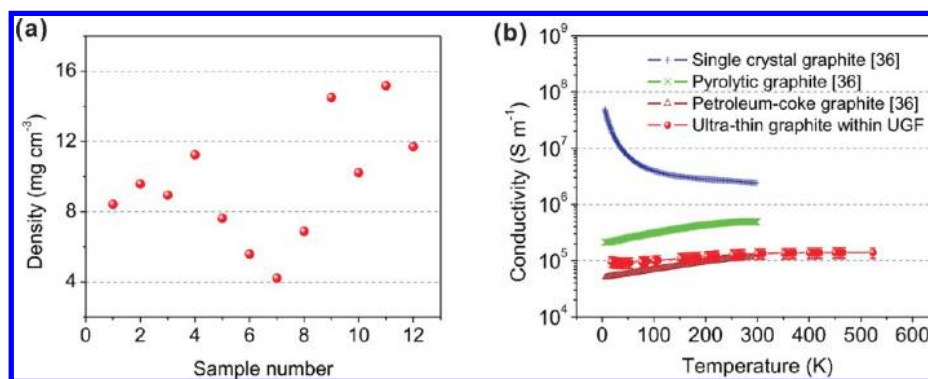


Figure 2. (a) Mass density dispersion of UGF measured from discs with diameters of ~ 7.6 mm and thicknesses of ~ 1.6 mm (dimensions and masses are listed in Supporting Information Table S1). (b) Electrical conductivity of the ultrathin graphite within the UGF at different temperatures. The error arises from uncertainty in the volume fraction. The basal-plane conductivities of petroleum-coke graphite, pyrolytic graphite, and single-crystal graphite are presented for comparison.³⁶

cm⁻³ and the solid electrical conductivity of the ultrathin graphite within the UGF is $\sim 1.3 \times 10^5$ S m⁻¹ at 300 K. Moreover, UGF presents excellent electrochemical stability comparing to that of Al and Ni at potentials of up to 5 V versus Li/Li⁺, which is favored for lithium ion batteries with high open-circuit voltage.

The UGF was prepared by precipitation of a very thin layer of graphite on Ni foam (Supporting Information Figure S1) and subsequent removal of the Ni (see Supporting Information). To obtain a robust UGF that can survive the electrode preparation, we exposed the nickel foam in CH₄ at 1050 °C for 1 h and subsequently cooled slowly. In this

procedure, carbon can saturate the nickel at 1050 °C and most of the C will precipitate at the surface of the nickel foam struts during the slow cooling, forming a continuous graphite coating with a wall thickness of tens of nanometers. This fabrication process differs from that reported by Chen et al.³⁰ in that the short exposure of nickel foam to CH₄ at high temperature and fast cooling yielded a graphene foam with wall thicknesses less than 10 graphene layers. Consequently, a polymethyl methacrylate (PMMA) supporting layer was needed when etching the nickel due to the weakness of the thin graphitic wall. We have found this step unnecessary for the thicker-walled UGF presented here. Also, PMMA residue is known to strongly

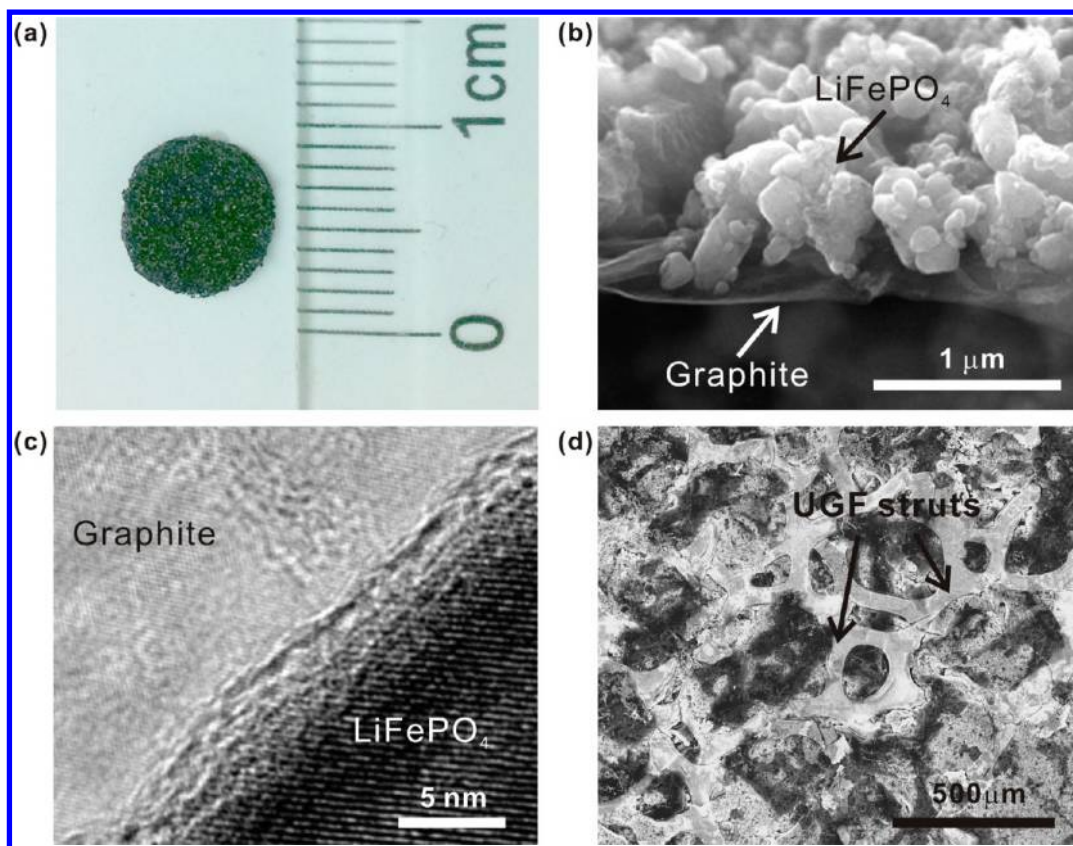


Figure 3. (a) Photograph of UGF loaded with LFP at a loading density of $\sim 12 \text{ mg cm}^{-2}$. (b) SEM image and (c) High-resolution TEM image of the UGF/LFP interface before compressing. (d) SEM image of the UGF/LFP electrode after being compressed at 10 MPa.

affect electron transport in graphene³¹ and adds a highly resistive interfacial layer between the UGF and the electrochemically active material. Figure 1a shows photographs of UGF pieces in different geometries, thus the size and shape of the UGF can be patterned to fit different applications. The UGF is that of a 3D interconnected network with struts having a width of around $50 \mu\text{m}$ and a pore size of $200\text{--}500 \mu\text{m}$ (Figure 1b). The hollow space inside that can be seen in Figure 1c is the result of the Ni foam structure (Supporting Information Figure S1) and the deposition of thin graphite. The Raman spectrum and X-ray diffraction (XRD) (Supporting Information Figure S2b,c) of UGF matches well with those of high quality, defect-free graphite. The average wall thickness of UGF struts deduced from XRD is $17.3 \pm 2.9 \text{ nm}$ (see Supporting Information), which is consistent with that obtained by TEM (Figure 1d). The thermal gravimetric analysis (TGA, Supporting Information Figure S2d) shows that the weight loss of UGF in air occurred mostly in the range of $630\text{--}780 \text{ }^\circ\text{C}$, indicating a graphitic structure,^{32,33} and only 1.5 wt % residue is left after holding at $780 \text{ }^\circ\text{C}$ for 30 min. The Raman and XRD data together with the TGA measurements confirm the graphitic nature of the UGF.

The mass density of the UGF was calculated from the UGF discs (Supporting Information Table S1) and is presented in Figure 2a, which gives a density of $(9.5 \pm 3.3) \text{ mg cm}^{-3}$ and a volume fraction of $(0.42 \pm 0.15) \text{ vol } \%$. We measured the temperature-dependent electrical conductivity of a UGF strip, σ_{UGF} , at different temperatures using a four-probe direct current (dc) method and used the following approach of Lemlich³⁴ to obtain the solid conductivity of the ultrathin graphite itself within the UGF:

$$\sigma_{\text{G}} = 3\sigma_{\text{UGF}}/\phi_{\text{UGF}} \quad (1)$$

where σ_{UGF} is the electrical conductivity of UGF and ϕ_{UGF} is the volume fraction. The Lemlich model³⁴ has been shown to adequately describe electrical transport in low ϕ , open celled metal foams.³⁵ The conductivity of ultrathin graphite within the UGF as a function of temperature is displayed in Figure 2b along with the reported conductivities of various graphites for comparison.³⁶ σ_{G} reaches a minimum of $9.1 \times 10^4 \text{ S m}^{-1}$ at around 41 K and increases to $1.3 \times 10^5 \text{ S m}^{-1}$ at room temperature. The error in σ_{G} arises from uncertainty in the volume fraction. The conductivity of ultrathin graphite is on the order of pyrolytic graphite,³⁶ though it is almost 2 orders of magnitude lower than that of single-crystal graphite.³⁶ The good electrical conductivity is indicative of efficient charge transfer between the UGF and the electrically active materials.

To test the performance of UGF as the 3D conductive network in an electrochemical cell, we conducted proof-of-concept studies based on the LFP³⁷ nanoparticles as the electrochemically active material. We prepared the UGF/LFP electrode by drop-casting an electrode slurry containing LFP, carbon black, and polyvinylidene fluoride (PVDF) at a weight ratio of 70:20:10 (wt %, dispersing in *N*-methyl-2-pyrrolidone as the solvent) onto a UGF disk with diameter of $\sim 7.6 \text{ mm}$ and thickness of $\sim 1.6 \text{ mm}$ and then drying at $80 \text{ }^\circ\text{C}$ in vacuum, which is quite similar to the process commonly used in industry where slurry is cast on a metal foil.³⁸ No significant deformation of the UGF occurred during electrode preparation (Figure 3a), indicative of the mechanical strength of UGF. The LFP particles disperse around the surface of the UGF struts (Figure 3b) and strongly adhere to them (Figure 3c). The UGF/LFP

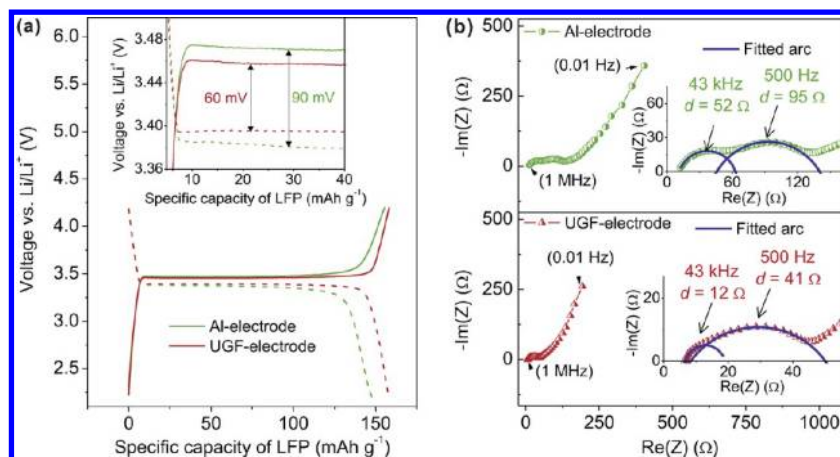


Figure 4. (a) The dc charge (solid line)/discharge (dashed line) profile of UGF- and Al-electrode (red and green lines, respectively). The inset presents the hysteresis between charge and discharge curves. (b) Nyquist plots of UGF- and Al-electrode, respectively. The insets show two arcs centered at around 43 kHz and 500 Hz, respectively, together with the fitted arcs that are obtained by electrochemical circle fitting. The loading densities of LFP on UGF- and Al-electrode were $\sim 12 \text{ mg cm}^{-2}$.

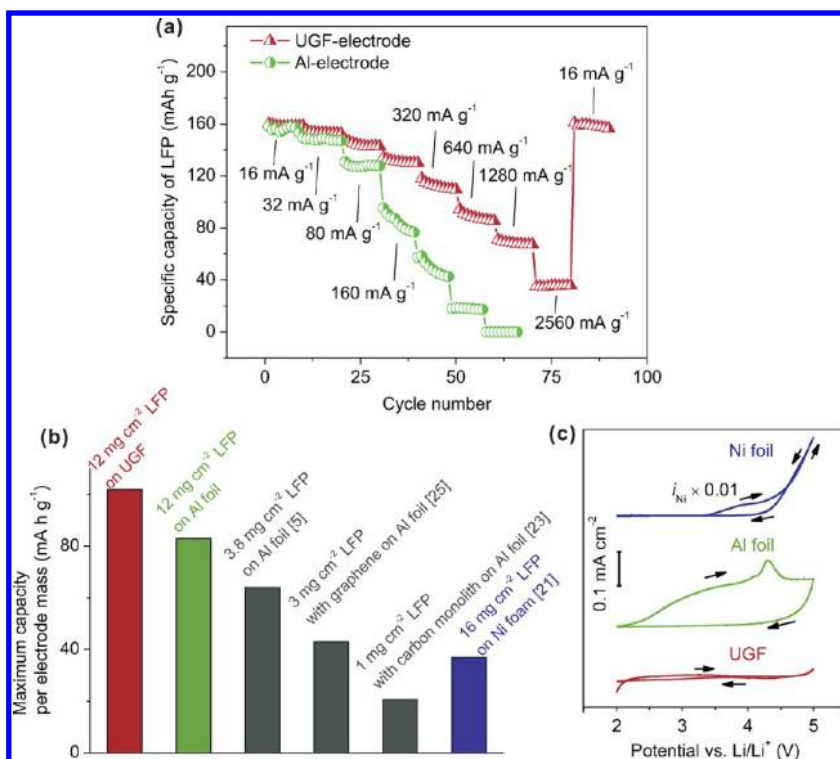


Figure 5. (a) Comparison of the specific capacities of UGF- and Al-electrode, respectively, with a LFP loading of $\sim 12 \text{ mg cm}^{-2}$ at different charge/discharge current densities. (b) Maximum specific capacity per electrode mass of UGF-electrode shown in comparison with that of Al-electrode of this work and previous reports using LFP on Al foil at lower loadings^{5,23,25} as well as LFP on Ni foam.²¹ (c) Cyclic voltammetry of UGF, Al and Ni foil measured at scan rate of 10 mV s^{-1} with 1 M LiPF_6 in EC/DMC (1:1 by volume) as the electrolyte and Li foil as the counter/reference electrode.

electrode was compressed when assembling cells, which yielded a $\sim 160 \mu\text{m}$ thick electrode ($\sim 14 \mu\text{m}$ thick of UGF without LFP). The struts remain continuous and are embedded in the electrode (Figure 3d). There were no additional metallic current collectors used in the cell assembly. For comparison, we drop-casted the electrode slurry onto a $20 \mu\text{m}$ thick aluminum foil which is commonly used in lithium ion batteries.³⁸ The loading densities of LFP on both the UGF and Al foil were $\sim 12 \text{ mg cm}^{-2}$. The electrodes of LFP on UGF and Al foil are referred to as UGF-electrode and Al-electrode, respectively.

The electrochemical performance of both the UGF- and Al-electrode was tested in a CR2032 coin-type cell after initializing the freshly prepared cells by holding them at the open circuit voltage for 12 h followed by dc charge/discharge at a current density of 16 mA g^{-1} for 3 cycles. The electrodes show a flat plateau at around 3.4 V in both dc charge and discharge curves of the first cycle (Figure 4a), which is characteristic of LFP.³⁷ Although the specific charge capacities of the UGF- and Al-electrode are close to the theoretical capacity (170 mAh g^{-1}) of LFP, the Coulombic efficiency of UGF-electrode (99.9%) is higher than that of the Al-electrode (95.0%), and the hysteresis

between the charge and the discharge curves of the UGF-electrode is 30% less than that of the Al-electrode. This result implies improved electrochemical reaction kinetics and can be mainly attributed to (i) the lower electron-transfer resistivity from LFP to the outer circuit and (ii) the higher active surface area of LFP in contact with the electrolyte.³⁹

We further evaluated the UGF-electrode by alternating current (ac) impedance spectroscopy to understand the improved electrochemical reaction kinetics. The sum of the resistance originating from the electrolyte, metallic leads, and other so-called "ohmic contributions", R_0 , can be read as the real part of the impedance, $\text{Re}(Z)$, at the highest frequency when the imaginary part of the impedance, $\text{Im}(Z)$, is zero, which is around 10 Ω for both the UGF- and Al-electrode, indicating a good assembly quality of the cells.⁴⁰ There are two arcs centered at frequencies of around 43 kHz and 500 Hz, respectively, for each electrode. The arcs centered at around 43 kHz can be attributed to the contact resistance between the LFP and the conductive substrate (here the UGF and Al foil, respectively) coupled with the double-layer capacitance created at the interface between the conductive substrate and the electrolyte; and the arcs centered at around 500 Hz can be explained as the charge-transfer resistance coupled with the double-layer capacitance between the LFP particles and the electrolyte.⁴¹ The resistances in the electrodes are determined through the arcs diameter,⁴¹ which is obtained by electrochemical circle fitting (see Supporting Information). The sum of the resistances obtained from the Nyquist plots is 53 Ω for the UGF-electrode and 147 Ω for the Al-electrode, respectively. The linear tail in the Nyquist plots at the low frequency is due to chemical diffusion of Li^+ inside the LFP particles, in which region the effective electrode surface area can be determined by the approach of Ho et al.⁴² The effective electrode surface area of the UGF-electrode is three times higher than that of the Al-electrode, as described in the Supporting Information. A low charge-transfer resistance and high effective surface of the electrode are favored for electron conduction and Li^+ migration, especially at high charge/discharge rates. Therefore, we can expect the UGF-electrode to deliver a greater rate capability than that of the Al-electrode.

The cycle-dependent specific capacities of the UGF- and Al-electrodes charged/discharged at various current densities are shown in Figure 5a. We obtained specific capacities of 70 and 36 mAh g^{-1} at current densities of 1280 and 2560 mA g^{-1} , respectively, for the UGF-electrode, whereas the Al-electrode failed at these high charge/discharge rates. When setting the current density back to 16 mA g^{-1} , the UGF-electrode regains a specific capacity of 158 mAh g^{-1} , which is almost the same value of that delivered at the first 10 cycles. The rate capability presented in Figure 5a is lower than that of LFP reported in some studies;^{4,5} the rate capability is also a function of the preparation process, the stoichiometry, and the crystalline structure of the electrochemically active material. The UGF is compatible with various electrochemically active materials, thereby providing a path to produce a battery electrode with high rate capability. In addition, optimization of the microstructure of the UGF by using Ni foam with cell size down to tens of micrometers (close to the width of the struts) would yield UGF with smaller open cells, thus increasing the filling homogeneity of the conductive struts so as to improve the rate capability.

In addition, the UGF-electrode yields higher specific capacity per unit mass of the whole electrode compared to that of the

Al-electrode owing to the extremely low density of UGF, $\sim 9.5 \text{ mg cm}^{-3}$. If we include the mass of the whole electrode containing electrochemically active material, additives, and conductive substrate, the maximum specific capacity of the UGF-electrode is 102 mAh g^{-1} (Figure 5b), which is 23% higher than that of the Al-electrode and is 170% higher than that of LFP on Ni foam²¹ (Figure 5b). It is worth noting that a low areal loading density of LFP on the conductive substrate ($2\text{--}6 \text{ mg cm}^{-2}$)^{4,5,25} has been generally used for thinning electrodes to have high electrode conductivity, thus to obtain improved rate performance. However, this strategy sacrifices the total capacity of the electrode. For example, the LFP/graphene²⁵ and LFP/carbon-monolith²³ composites with LFP areal loading densities of 3 and 1 mg cm^{-2} , respectively, were used for achieving a better rate capability, which resulted in a poor maximum capacity of only 43 and 21 mAh g^{-1} , respectively (Figure 5b). For this reason, we use relatively high areal loading densities of ~ 12 , ~ 24 , and $\sim 36 \text{ mg cm}^{-2}$ of LFP on UGF, and the rate capabilities of the UGF-electrodes are still better than that of Al-electrode with lower LFP loading (Supporting Information Figure S3).

More importantly, UGF presents excellent electrochemical stability at high potentials versus Li/Li^+ . Both Al and Ni foil show intensive anodic current (Figure 5c) in the commercial electrolyte for lithium ion batteries owing to the formation of a passive layer and/or corrosion⁴³ and decomposition of LiPF_6 organic carbonate electrolytes,⁴⁴ which is in relation to the self-discharge of lithium ion batteries.⁴⁵ However, no anodic current for UGF is found in the potentials of 2–5 V (Figure 5c), which is favored for batteries with high open-circuit voltage. This result indicates excellent electrochemical stability and reversibility of the UGF-electrode, which is consistent with the high Coulombic efficiency of 99.5% over 60 cycles (Supporting Information Figure S4) and reflects a robust structure of the UGF-electrode after 50 charge/discharge cycles (Supporting Information Figure S5).

In summary, we have demonstrated a general method for creating high-rate capability rechargeable lithium ion batteries using a 3D interconnected network of ultrathin graphite foam. The free-standing, lightweight, and conductive ultrathin graphite foam presents excellent electrochemical stability in LiPF_6 -organic carbonate electrolytes at potentials up to 5 V versus Li/Li^+ and enhances both the rate capability and specific capacity of battery electrodes simultaneously. This method is independent from the electrochemically active material preparation process and therefore compatible with many lithium chemistries. Further optimization of the ultrathin graphite foam structure and electrode preparation would extend their application to other electrochemical energy storage devices, such as fuel cells and supercapacitors. Finally, the UGF-electrode fabrication is scalable and compatible with industrial manufacturing approaches.

■ ASSOCIATED CONTENT

📄 Supporting Information

Experimental details, SEM images, Raman spectrum, X-ray diffraction and electrochemical data of samples. This material is available free of charge via the Internet at <http://pubs.acs.org>.

■ AUTHOR INFORMATION

Corresponding Author

*E-mail: r.ruoff@mail.utexas.edu

Notes

The authors declare no competing financial interest.

■ ACKNOWLEDGMENTS

We appreciate support from the U.S. Department of Energy (DOE) under award DE-SC001951 and ARPA-E contract DE-AR0000178. We also thank Prof. Dr. Yuguo Guo, Prof. Dr. Anmin Cao, and Dr. Maowen Xu for helpful discussion.

■ REFERENCES

- (1) Armand, M.; Tarascon, J. M. *Nature* **2008**, *451*, 652–657.
- (2) Maier, J. *Nat. Mater.* **2005**, *4*, 805–815.
- (3) Tarascon, J. M.; Armand, M. *Nature* **2001**, *414*, 359–367.
- (4) Chung, S. Y.; Bloking, J. T.; Chiang, Y. M. *Nat. Mater.* **2002**, *1*, 123–128.
- (5) Kang, B.; Ceder, G. *Nature* **2009**, *458*, 190–193.
- (6) Wang, Y.; Wang, Y.; Hosono, E.; Wang, K.; Zhou, H. *Angew. Chem., Int. Ed.* **2008**, *47*, 7461–7465.
- (7) Fu, L. J.; Liu, H.; Li, C.; Wu, Y. P.; Rahm, E.; Holze, R.; Wu, H. Q. *Solid State Sci.* **2006**, *8*, 113–128.
- (8) Ji, H.-X.; Wu, X.-L.; Fan, L.-Z.; Krien, C.; Fiering, I.; Guo, Y.-G.; Mei, Y.; Schmidt, O. G. *Adv. Mater.* **2010**, *22*, 4591–4595.
- (9) Bruce, P. G.; Scrosati, B.; Tarascon, J.-M. *Angew. Chem., Int. Ed.* **2008**, *47*, 2930–2946.
- (10) Guo, Y.-G.; Hu, J.-S.; Wan, L.-J. *Adv. Mater.* **2008**, *20*, 2878–2887.
- (11) Manthiram, A.; Murugan, A. V.; Sarkar, A.; Muraliganth, T. *Energy Environ. Sci.* **2008**, *1*, 621–638.
- (12) Chan, C. K.; Peng, H.; Liu, G.; McIlwrath, K.; Zhang, X. F.; Huggins, R. A.; Cui, Y. *Nat. Nanotechnol.* **2008**, *3*, 31–35.
- (13) Long, J. W.; Dunn, B.; Rolison, D. R.; White, H. S. *Chem. Rev.* **2004**, *104*, 4463–4492.
- (14) Rolison, D. R.; Long, R. W.; Lytle, J. C.; Fischer, A. E.; Rhodes, C. P.; McEvoy, T. M.; Bourga, M. E.; Lubers, A. M. *Chem. Soc. Rev.* **2009**, *38*, 226–252.
- (15) Ergang, N. S.; Lytle, J. C.; Lee, K. T.; Oh, S. M.; Smyrl, W. H.; Stein, A. *Adv. Mater.* **2006**, *18*, 1750–1753.
- (16) Zhang, H.; Yu, X.; Braun, P. V. *Nat. Nanotechnol.* **2011**, *6*, 277–281.
- (17) Cao, F.-F.; Deng, J.-W.; Xin, S.; Ji, H.-X.; Schmidt, O. G.; Wan, L.-J.; Guo, Y.-G. *Adv. Mater.* **2011**, *23*, 4415–4420.
- (18) Taberna, L.; Mitra, S.; Poizot, P.; Simon, P.; Tarascon, J. M. *Nat. Mater.* **2006**, *5*, 567–573.
- (19) Ji, X.; Lee, K. T.; Nazar, L. F. *Nat. Mater.* **2009**, *8*, 500–506.
- (20) Shi, Y.; Guo, B.; Corr, S. A.; Shi, Q.; Hu, Y.-S.; Heier, K. R.; Chen, L.; Seshadri, R.; Stucky, G. D. *Nano Lett.* **2009**, *9*, 4215–4220.
- (21) Yao, M.; Okuno, K.; Iwaki, T.; Kato, M.; Tanase, S.; Emura, K.; Sakai, T. *J. Power Sources* **2007**, *173*, 545–549.
- (22) Shin, H. C.; Liu, M. L. *Adv. Funct. Mater.* **2005**, *15*, 582–586.
- (23) Doherty, C. M.; Caruso, R. A.; Smarsly, B. M.; Adelman, P.; Drummond, C. J. *Chem. Mater.* **2009**, *21*, 5300–5306.
- (24) Hasegawa, G.; Ishihara, Y.; Kanamori, K.; Miyazaki, K.; Yamada, Y.; Nakanishi, K.; Abe, T. *Chem. Mater.* **2011**, *23*, 5208–5216.
- (25) Wang, H.; Yang, Y.; Liang, Y.; Cui, L.-F.; Casalongue, H. S.; Li, Y.; Hong, G.; Cui, Y.; Dai, H. *Angew. Chem., Int. Ed.* **2011**, *50*, 7364–7368.
- (26) Wang, D.; Choi, D.; Li, J.; Yang, Z.; Nie, Z.; Kou, R.; Hu, D.; Wang, C.; Saraf, L. V.; Zhang, J.; Aksay, I. A.; Liu, J. *ACS Nano* **2009**, *3*, 907–914.
- (27) Zhou, Y.; Wang, J.; Hu, Y.; O’Hayre, R.; Shao, Z. *Chem. Commun.* **2010**, *46*, 7151–7153.
- (28) Lee, S. W.; Yabuuchi, N.; Gallant, B. M.; Chen, S.; Kim, B.-S.; Hammond, P. T.; Shao-Horn, Y. *Nat. Nanotechnol.* **2010**, *5*, 531–537.
- (29) Reddy, A. L. M.; Shaijumon, M. M.; Gowda, S. R.; Ajayan, P. M. *Nano Lett.* **2009**, *9*, 1002–1006.
- (30) Chen, Z.; Ren, W.; Gao, L.; Liu, B.; Pei, S.; Cheng, H.-M. *Nat. Mater.* **2011**, *10*, 424–428.
- (31) Bolotin, K. I.; Sikes, K. J.; Jiang, Z.; Klima, M.; Fudenberg, G.; Hone, J.; Kim, P.; Stormer, H. L. *Solid State Commun.* **2008**, *146*, 351–355.
- (32) Hata, K.; Futaba, D. N.; Mizuno, K.; Namai, T.; Yumura, M.; Iijima, S. *Science* **2004**, *306*, 1362–1364.
- (33) Su, F.; Zeng, J.; Bao, X.; Yu, Y.; Lee, J. Y.; Zhao, X. S. *Chem. Mater.* **2005**, *17*, 3960–3967.
- (34) Lemlich, R. J. *Colloid Interface Sci.* **1978**, *64*, 107–110.
- (35) Goodall, R.; Weber, L.; Mortensen, A. *J. Appl. Phys.* **2006**, *100*, 044912.
- (36) Klein, C. A. *Rev. Mod. Phys.* **1962**, *34*, 56–79.
- (37) Padhi, A. K.; Nanjundaswamy, K. S.; Goodenough, J. B. *J. Electrochem. Soc.* **1997**, *144*, 1188–1194.
- (38) Whitehead, A. H.; Schreiber, M. *J. Electrochem. Soc.* **2005**, *152*, A2105–A2113.
- (39) Dominko, R.; Bele, M.; Gaberscek, M.; Remskar, M.; Hanzel, D.; Goupil, J. M.; Pejovnik, S.; Jamnik, J. *J. Power Sources* **2006**, *153*, 274–280.
- (40) Doyle, M.; Meyers, J. P.; Newman, J. *J. Electrochem. Soc.* **2000**, *147*, 99–110.
- (41) Gaberscek, M.; Moskon, J.; Erjavec, B.; Dominko, R.; Jamnik, J. *Electrochem. Solid State Lett.* **2008**, *11*, A170–A174.
- (42) Ho, C.; Raistrick, I. D.; Huggins, R. A. *J. Electrochem. Soc.* **1980**, *127*, 343–350.
- (43) Myung, S. T.; Hitoshi, Y.; Sun, Y. K. *J. Mater. Chem.* **2011**, *21*, 9891–9911.
- (44) Geoffroy, I.; Willmann, P.; Mesfar, K.; Carre, B.; Lemordant, D. *Electrochim. Acta* **2000**, *45*, 2019–2027.
- (45) Zhang, S. S.; Ding, M. S.; Jow, T. R. *J. Power Sources* **2001**, *102*, 16–20.